ACS APPLIED MATERIALS & INTERFACES

Research Article

www.acsami.org

Facile Preparation of Molybdenum Bronzes as an Efficient Hole Extraction Layer in Organic Photovoltaics

Jiantai Wang,[†,‡] Jun Zhang,[†,‡] Bin Meng,[†,‡] Baohua Zhang,[†] Zhiyuan Xie,*[,†] and Lixiang Wang[†]

[†]State Key Laboratory of Polymer Physics and Chemistry, Changchun Institute of Applied Chemistry, Chinese Academy of Sciences, Changchun 130022, P. R. China

[‡]University of Chinese Academy of Sciences, Beijing 100039, P. R. China

Supporting Information

ABSTRACT: We proposed a facile and green one-pot strategy to synthesize Mo bronzes nanoparticles to serve as an efficient hole extraction layer in polymer solar cells. Mo bronzes were obtained through reducing the fractional self-aggregated ammonium heptamolybdate with appropriate reducing agent ascorbic acid, and its optoelectronic properties were fully characterized. The synthesized Mo bronzes displayed strong n-type semiconductor characteristics with a work function of 5.2−5.4 eV, matched well with the energy levels of current donor polymers. The presented gap states of the Mo bronzes near the Fermi level were beneficial for facilitating charge extraction. The as-synthesized Mo bronzes were used as hole extraction layer in polymer solar cells and significantly enhanced the photovoltaic performance and stability. The power conversion efficiency was increased by more than 18% compared with the polyethylene dioxythiophene:polystyrenesulfonate-based reference cell. The excellent performance and facile preparation render the as-synthesized solution-processed Mo bronzes nanoparticles a promising candidate for hole extraction layer in low-cost and efficient polymer solar cells.

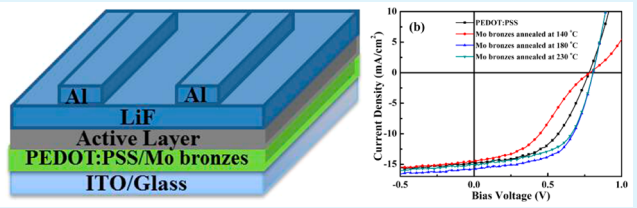

KEYWORDS: *organic photovoltaics, hole extraction layer, Mo bronzes, solution-processing, stability*

1. INTRODUCTION

Fueled by the growing concerns on energy security and global warming, organic photovoltaic (OPV) cells are considered to be a potential green and renewable energy technology as one of alternatives to fossil fuel-based technologies.[1,2] Over the past two decades, OPVs have attracted a great deal of attention because of their unique features such as cost-effective, solution-processing, lightweight, high-throughput production, etc.[3−9] Significant advances have been gained along with the progress in photoactive materials and device engineering.[10−15] One of the pivotal components in bulk heterojunction (BHJ) OPV devices is the interfacial layers between the active layer and electrodes, which would facilitate the charge extraction.[16−18] As the linker of adjoining components, the interfacial layers also significantly affect the stability of OPV devices.[19,20] Developing a straightforward method to prepare more effective charge selective interlayers is highly desirable for the low-cost, high-throughput manufacturing of efficient OPV modules.

Currently, the aqueous polyethylene dioxythiophene:polystyrenesulfonate (PEDOT:PSS) solution is widely used as the hole extraction layer in OPVs.[21,22] However, the hygroscopic nature of PEDOT:PSS has a detrimental impact on device stability, and its acidic nature is also prone to etch the indium tin oxide (ITO) electrode and the contacted interfaces, severely limiting the large-scale commercial usage.[23−25] In this regard, transition metal oxide semiconductors, such as MoO_3,[18,26−36] NiO,[37−40] V_2O_5,[41,42] and WO_3,[43,44] are emerging as a promising class of alternatives for PEDOT:PSS, with demonstrable advantages of the wide range of energy level aligning capabilities,[26] high transmittance in the visible region,[45,46] and excellent ambient stability.[47] Moreover, the developed solution-processed metal oxides semiconductors are compatible with low-cost all-solution high-throughput manufacturing of OPVs. Among these semiconductor nanoparticles, solution-processed MoO_3 has been prepared from different precursors and proved to be a promising candidate as efficient hole extraction layer. Previous studies mainly focused on the fully stoichiometric MoO_3 using the high temperature annealing process.[48] More recent studies showed that partially reduced MoO_3, namely hydrogen molybdenum bronzes (Mo bronzes), exhibited superior performance in OPV devices.[18,26,31]

Herein, we proposed a facile and green one-pot method to synthesize solution-processed Mo bronzes nanoparticles to serve as the hole extraction layer in polymer solar cells. The solution-processed Mo bronzes nanoparticles were obtained by reducing the fractional self-aggregated ammonium heptamolybdate with appropriate reducing agent ascorbic acid at ambient conditions, and the solution of Mo bronzes was stable for at least one month. Strikingly, the device performance was prominently improved by implementing Mo bronzes as anode interfacial layer in OPVs, regardless of the donor−acceptor

Received: April 8, 2015
Accepted: June 2, 2015
Published: June 10, 2015

DOI: 10.1021/acsami.5b02997
ACS Appl. Mater. Interfaces 2015, 7, 13590−13596

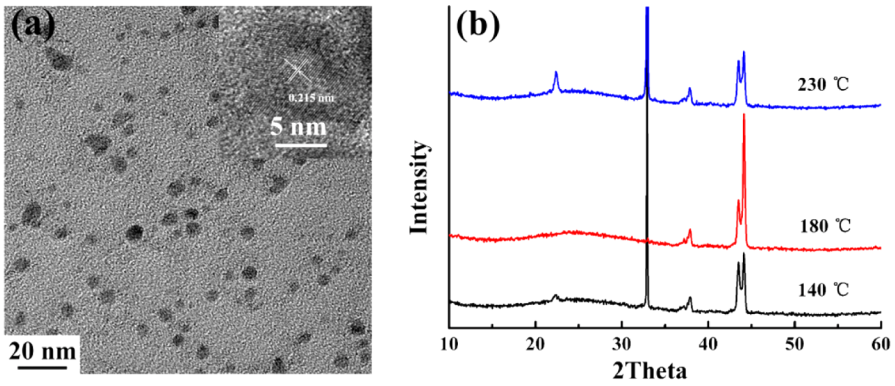

Figure 1. (a) The representative TEM image of the solution-processed Mo compounds. The scale bar is 20 nm. Inset: HRTEM image of the Mo bronzes. (b) XRD patterns of the samples annealed at 140, 180, and 230 °C, respectively.

combination. The power conversion efficiency (PCE) value increased from 5.11% for the PEDOT:PSS-based device to 6.02% for the Mo bronzes-based device using the poly[N-9″-hepta-decanyl-2,7-carbazole-*alt*-5,5-(4′,7′-di-2-thienyl-2′,1′,3′-benzothiadiazole)]:[6,6]-phenyl-C_{71} butyric acid methyl ester (PCDTBT:$PC_{71}BM$) blend as the active layer. Additionally, the stability of unencapsulated devices was greatly improved by using Mo bronzes to replace PEDOT:PSS.

2. EXPERIMENTAL SECTION

2.1. Materials Preparation. Briefly, ammonium heptamolybdate (0.9888 g) was dissolved in deionized water (80 mL) to form a clear solution (0.01 M). The pH value of the solution was adjusted between 3 and 4 using HCl and then incubated at room temperature for 12 h. Subsequently, the ascorbic acid solution (0.01 M, 1 mL) was added dropwise into the ammonium heptamolybdate solution (0.01 M, 20 mL) under stirring. The reaction mixture was stirred at 30 °C under air for 8 h. The solution color turned slowly from colorless to blue, which indicated that the Mo^{6+} ions were partially reduced to Mo^{5+}. The prepared solution was directly used to fabricate OPV devices.

2.2. Device Fabrication and Measurements. The ITO-coated glass with a sheet resistance of 10 Ω/□ was used as the substrate, which was cleaned ultrasonically in acetone and isopropyl alcohol each for 15 min and then rinsed with deionized water three times. The cleaned ITO substrates were dried in an oven at 120 °C for 1 h and subsequently were treated with UV-Ozone for 25 min. The PEDOT:PSS (Baytron Al 4083) or the prepared Mo bronzes solution was spin-coated on the ITO glass substrate, and their thicknesses were about 30 and 10 nm, respectively. The PEDOT:PSS-coated substrates were annealed at 140 °C for 30 min, and the Mo bronzes nanoparticles-coated substrates were annealed at different temperatures for 10 min on a hot plate at ambient condition. Then the substrates were transferred into a glovebox to spin-coat the active layer. The solutions of PCDTBT:$PC_{71}BM$ (1:4 in weight, 3.5 mg/mL) in 1,2-dichlorobenzene (DCB) or PBDTTT-C-T:$PC_{71}BM$ (1:1.5 in weight, 10 mg/mL) in DCB containing 3% (v/v) 1,8-diiodooctane (DIO) were spin-coated to prepare the active layer. Finally, a cathode structure of LiF (~0.8 nm)/Al (100 nm) was thermally evaporated in a vacuum chamber at a base pressure of 4×10^{-6} Torr. The active area of cell was about 12 mm^2, defined by the overlapping area of the ITO and Al electrodes. A Newport simulator with an AM1.5G filter was used to provide 100 mW cm^{-2} simulated solar light for illumination of the photovoltaic cells. The light intensity was determined by using a calibrated silicon diode with a KG-5 visible color filter. Current–voltage ($J - V$) characteristics of the cells were measured with a Keithley 236 source meter under ambient condition. The external quantum efficiency (EQE) was measured using an Enlitech QE-R spectral response measurements system illuminated with bias white light under short-circuit conditions.

2.3. Thin Film Characterization. The thicknesses of the various films were measured with a Dektak 6 M Stylus Profiler. Transmittance spectra of the samples were obtained using a PerkinElmer 35 UV–vis spectrophotometer. The X-ray photoelectron spectroscopy (XPS) measurements were carried out on a Thermo ESCALAB 250 using monochromatized Al Kα ($h\nu$ = 1486.8 eV) excitation. The ultraviolet photoelectron spectroscopy (UPS) measurements were carried out with a helium discharge lamp excitation (21.2 eV) and a hemispherical energy analyzer (Specs PHOIBOS 150). The samples were biased at −10 V to separate the sample and the secondary edge for the analyzer. The transmission electron microscopy (TEM) and high-resolution TEM (HRTEM) images were recorded using a FEI TECNAI F20 system operated at an acceleration voltage of 200 kV. The atomic force microscopy (AFM) images were taken on a SPA-300HV instrument with a SPI3800N Controller operating in the tapping mode. Thin-film X-ray diffraction (XRD) was carried out using a Bruker D8 Discover thin-film diffractometer with Cu Kα radiation (λ = 1.5406 Å) operated at 40 kV and 30 mA in reflection mode.

3. RESULTS AND DISCUSSION

The Mo bronzes nanoparticles were readily prepared by reduction of aggregated ammonium heptamolybdate using ascorbic acid. HCl was first added to the ammonium heptamolybdate solution in water to adjust pH value between 3 and 4. Under acid condition, ammonium heptamolybdate can be self-aggregated to form polymolybdate nanoparticles. The polymolybdate nanoparticles were partially reduced to form Mo bronzes with addition of ascorbic acid. Figure 1, panel a displays the typical TEM image of the resultant Mo bronzes nanoparticles with the inset showing the HRTEM image. The synthesized Mo bronzes appeared as spherical particles and had a good monodispersity with the average diameter of 4.52 ± 1.18 nm. The size distribution of Mo bronzes was shown in Figure S1 of the Supporting Information. The HRTEM image revealed lattice fringes with an interplanar spacing of 0.215 nm, in accord with (−621) diffraction plane of monoclinic Mo_4O_{11} (JCPDS 13–0142). Figure 1, panel b shows XRD patterns of the as-prepared Mo bronzes annealed at different temperatures. The three samples displayed similar typical peaks, which were indexed as blends of $MoO_3 \cdot 0.5H_2O$ and Mo_4O_{11} phase. The peaks at 2θ = 37.904° and 43.297° matched the (−103) and (−303) diffraction planes of monoclinic $MoO_3 \cdot 0.5H_2O$ (space group $P2_{1/m}$, JCPDS no. 49–0652), respectively, whereas the peaks at 2θ = 37.141° and 44.060° consisted with (−612) and (−1002) diffraction planes of monoclinic Mo_4O_{11} (space group $P2_{1/a}$, JCPDS no. 13–0142).

The AFM image of the spin-coated Mo bronzes layer on the ITO substrate was given in Figure S2 of the Supporting

DOI: 10.1021/acsami.5b02997
ACS Appl. Mater. Interfaces 2015, 7, 13590–13596

Information. Root−mean−square (RMS) roughness of the Mo bronzes layer was about 1.18 nm, much smoother than 7.2 nm of the bare ITO substrate. Although the Mo bronzes layer seems to have some small pinholes, it does not have detrimental effects on the photovoltaic performance of the resulted devices, as discussed later. XPS analysis was further employed to characterize the surface chemical composition of the obtained Mo bronzes films annealed at different temperatures. Figure 2, panels a−c show the Mo 3d spectra of the Mo

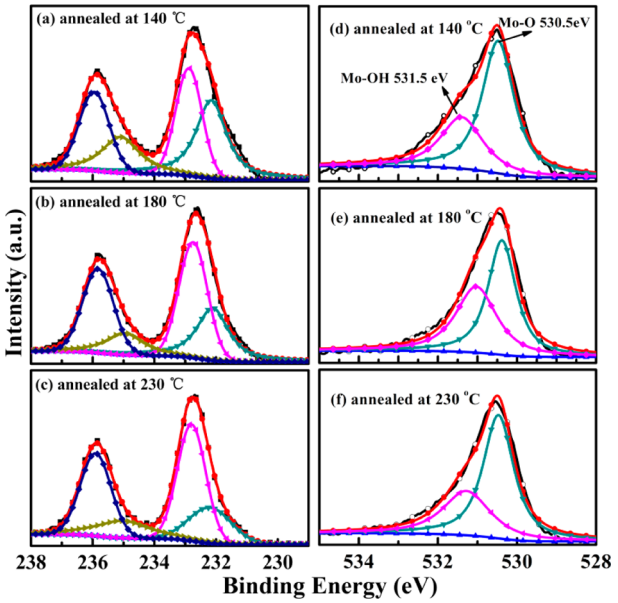

Figure 2. XPS spectra of Mo bronzes films annealed at different temperatures, respectively. Left panel: Mo 3d core level, (a) 140 °C, (b) 180 °C, (c) 230 °C. Right panel: O 1s spectra, (d) 140 °C, (e) 180 °C, (f) 230 °C.

bronzes films annealed at different temperatures. The Mo 3d core level peaks were deconvoluted into two doublets in form of Gaussian−Lorentzian curves, suggesting the coexistence of two different oxidation states Mo^{5+} and Mo^{6+} of molybdenum. The dominant peaks at 232.8 and 236 eV were ascribed to the $3d_{3/2}$ and $3d_{5/2}$ core level components for the Mo^{6+},[49] while the smaller peaks at 231.9 and 235.4 eV were attributed to the Mo^{5+}.[50] With elevating the annealing temperature from 140 to 230 °C, the surface content of Mo^{5+} is gradually decreased relative to Mo^{6+} content, indicating that some Mo^{5+} is oxidized at higher annealing temperature. The XPS spectra of O 1s exhibited asymmetric bands, as shown in Figure 2, panels d−f. However, as reported, the O 1s peak generally appears between 529.5 and 530.5 eV in transition metal oxides.[51] The O 1s peaks of the Mo bronzes films were fitted into two peaks at 530.5 and 531.5 eV, which were assigned to Mo−O bond and hydroxyl groups bonded to metal atoms (Mo−OH),[52] respectively.

As an anode interfacial layer, the surface electronic structure of the as-synthesized Mo bronzes may strongly influence its contact with the active layer and hence the final photovoltaic performance of the polymer solar cells (PSCs). Figure 3, panel a shows the secondary electron cutoff region of the UPS spectra from the Mo bronzes annealed at different temperatures with the commonly used PEDOT:PSS as reference. The work functions (W_F) of individual films are calculated from their corresponding values of secondary electron cutoff. The Mo bronzes displayed comparable or higher W_F values (5.2−5.4

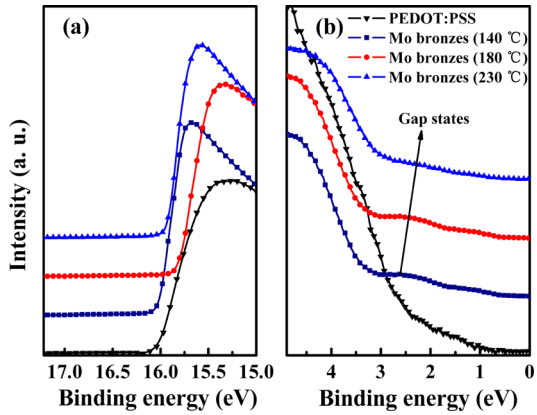

Figure 3. UPS spectra of Mo bronzes films measured at three annealed temperature. The UPS spectra of PEDOT:PSS were shown for comparison. (a) Secondary electron cut-off region, (b) density of states near the VB edge.

eV) than that of the PEDOT:PSS, especially for those annealed at higher temperatures. However, these W_F values do not show distinctly linear dependence on the Mo^{5+} content on the Mo bronzes surface. The corresponding density of states near the valence band (VB) edge spectra of those samples are 2.90, 3.16, and 3.20 eV below the Fermi level, respectively, for the Mo bronzes annealed at 140, 180, and 230 °C (Figure 3b). Therefore, the ionization energies (IEs) of the Mo bronzes were estimated to be 8.10, 8.56, and 8.49 eV, respectively. A set of gap states near the Fermi level were presented for the Mo bronzes (Figure 3b). These gap states were originated from the O vacancies and inserted hydrogen atoms in molybdenum oxide. The intervalence electrons were transferred from hydrogen atoms, which formed covalent bonds with oxygen atoms in the hydrogen molybdenum bronzes, to the initially empty Mo 4d states.[53,54] The optical band gap (E_g) of the Mo bronzes was about 3.65−3.75 eV derived from Tauc's formula (Figure S3, Supporting Information). On the basis of these results, the corresponding energy level diagram for the fabricated PSCs is presented in Figure 4. Compared with the PEDOT:PSS, the W_F values of the Mo bronzes were higher in favor of increasing the local electric field and thereby facilitating the hole extraction. Furthermore, n-type characteristic of the Mo bronzes was also important for their application. Owing to the deep VB edge of the Mo bronzes and large hole barriers at the Mo bronzes/polymer donor interfaces, it was not possible for holes to be extracted via VB of the Mo bronzes. The gap states of the Mo bronzes near the Fermi level would provide a profitable path for the hole extraction.

The photovoltaic properties of PSCs using the Mo bronzes annealed at different temperatures as the hole extraction layer were evaluated. These devices had the basic structure of ITO/Mo bronzes or PEDOT:PSS/active layer/LiF/Al, as illustrated in Figure 4. The blends of PCDTBT:$PC_{71}BM$ and PBDTTT-C-T:$PC_{71}BM$ are selected to serve as the active layer since the PCDTBT and PBDTTT-C-T are representative wide and narrow bandgap polymer donors, respectively. The illuminated $J-V$ characteristics of the PSCs based on the PCDTBT:$PC_{71}BM$ or PBDTTT-C-T:$PC_{71}BM$ blends are depicted in Figure 5, panels a and b, respectively, and their detailed photovoltaic parameters are summarized in Table 1. As seen in Figure 5, panel a, all the PCDTBT:$PC_{71}BM$ PSCs with the Mo bronzes annealed at different temperatures showed

DOI: 10.1021/acsami.5b02997
ACS Appl. Mater. Interfaces 2015, 7, 13590−13596

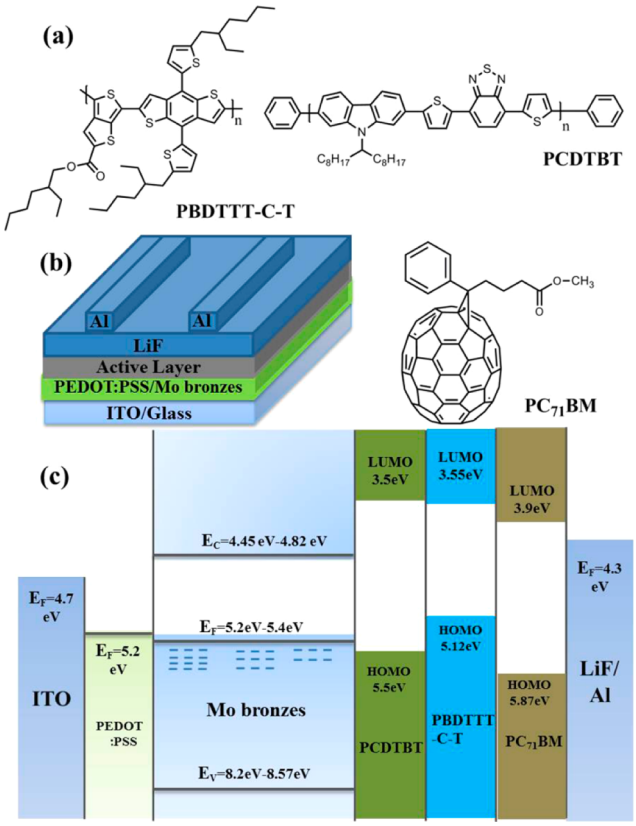

Figure 4. (a) Molecular structures of PBDTTT-C-T, PCDTBT, and $PC_{71}BM$. (b) Device structure of the OPVs. (c) Energy diagram of the materials involved in the OPVs.

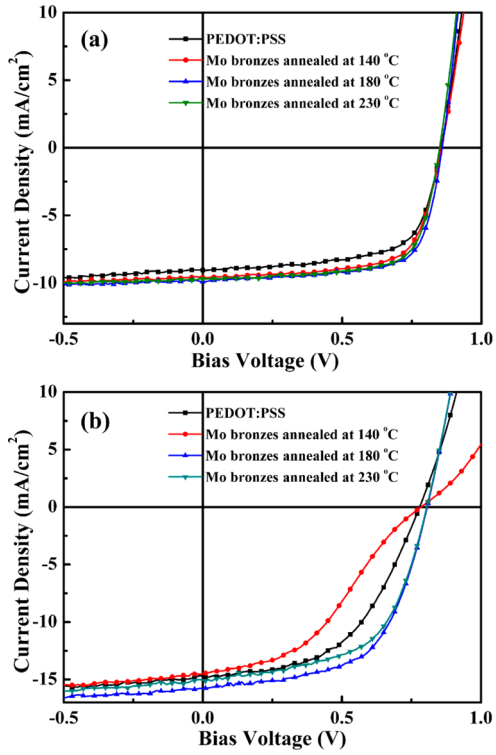

Figure 5. Illuminated $J-V$ characteristics of the (a) PCDTBT:$PC_{71}BM$ and (b) PBDTTT-C-T:$PC_{71}BM$ PSCs using Mo bronzes annealed at different temperatures as anode interfacial layer. The reference PSCs using PEDOT:PSS as anode interfacial layer are included for comparison.

superior photovoltaic performances compared with the PEDOT:PSS-based control devices. Both the short-circuit current density (J_{SC}) and fill factor (FF) were significantly increased with Mo bronzes to replace the PEDOT:PSS. For example, the PEDOT:PSS-based PCDTBT:$PC_{71}BM$ PSCs showed an open-circuit voltage (V_{OC}) of 0.85 V, a J_{SC} of 9.05 mA/cm^2, and a FF of 66.4%, leading to an overall PCE of 5.11%. When the Mo bronzes annealed at 180 °C was used to replace the PEDOT:PSS, the resultant PSC showed a V_{OC} of 0.86 V, a J_{SC} of 9.88 mA/cm^2, and a FF of 70.9%, giving a PCE of 6.02%. The EQE spectra of these devices are provided in Figure S4 of the Supporting Information. The calculated J_{SC} values of the PEDOT:PSS-based PCDTBT:$PC_{71}BM$ cell and the PCDTBT:$PC_{71}BM$ cells with Mo bronzes annealed at three different temperatures are 9.05, 9.65, 9.83, and 9.76 mA/cm^2, respectively, which are well matched with the measured values of 9.05, 9.59, 9.88, and 9.67 mA/cm^2. The Mo bronzes were also tested as hole extraction layer in the PBDTTT-C-T:$PC_{71}BM$ BHJ PSCs. As depicted in Figure 5, panel b, the PBDTTT-C-T:$PC_{71}BM$ BHJ cell with PEDOT:PSS anode interfacial layer demonstrated a V_{OC} of 0.78 V, a J_{SC} of 14.73 mA/cm^2, and a FF of 51.2%, resulting in an overall PCE of 5.89%. However, in contrast to the PCDTBT:$PC_{71}BM$ PSCs, the PBDTTT-C-T:$PC_{71}BM$ BHJ cells with Mo bronzes as anode interfacial layer are very sensitive to the annealing temperatures of the Mo bronzes. The Mo bronzes annealed at 140 °C may result in large interfacial resistance with PBDTTT-C-T donor and thus inferior photovoltaic performance of the PBDTTT-C-T:$PC_{71}BM$ cell compared to the PEDOT:PSS-based control device. The photovoltaic performance of the

Table 1. Device Parameters of OPVs Based on the PCDTBT and PBDTTT-C-T System That Used PEDOT:PSS and Mo Bronzes as HTL

devices	V_{OC} (V)	J_{SC} (mA/cm^2)	FF (%)	PCE (%)
PCDTBT:$PC_{71}BM$				
PEDOT:PSS	0.85	9.05	66.4	5.11
Mo bronzes (140 °C)	0.86	9.59	68.4	5.64
Mo bronzes (180 °C)	0.86	9.88	70.9	6.02
Mo bronzes (230 °C)	0.86	9.67	70.4	5.85
PBDTTT-C-T:$PC_{71}BM$				
PEDOT:PSS	0.78	14.73	51.2	5.89
Mo bronzes (140 °C)	0.78	14.48	39.9	4.50
Mo bronzes (180 °C)	0.81	15.79	58.6	7.49
Mo bronzes (230 °C)	0.81	15.06	57.5	7.01

PBDTTT-C-T:$PC_{71}BM$ BHJ cells with Mo bronzes annealed at higher temperatures (180 and 230 °C) was dramatically enhanced compared with the PEDOT:PSS-based control device. For instance, the PBDTTT-C-T:$PC_{71}BM$ cell with Mo bronzes annealed at 180 °C showed the best photovoltaic performance with a V_{OC} of 0.81 V, a J_{SC} of 15.79 mA/cm^2, and a FF of 58.6%, giving a PCE of 7.49%. In fact, the effect of different temperature annealed Mo bronzes has similar trends on the photovoltaic performance of the PSCs based on the PCDTBT:$PC_{71}BM$ and PBDTTT-C-T:$PC_{71}BM$ blends, but with more pronounced influence on the PBDTTT-C-T:$PC_{71}BM$ PSCs. The highest photovoltaic performance is achieved with Mo bronzes annealed at 180 °C for the two kinds of PSCs. With further increasing the Mo bronzes annealing temperature to 230 °C, the photovoltaic performance of both

DOI: 10.1021/acsami.5b02997
ACS Appl. Mater. Interfaces 2015, 7, 13590−13596

the two kinds of solar cells is a little decreased. Although a little higher transmittance of Mo bronzes relative to the PEDOT:PSS may contribute to the J_{SC} enhancement to some extent (Figure S5, Supporting Information), the significant increase of FF indicated that the charge extraction efficiency was improved by using Mo bronzes to replace PEDOT:PSS.

The charge extraction efficiency is strongly correlated to the charge recombination status in the BHJ PSCs. The efficient interfacial layer may suppress the charge recombination and improve the charge extraction efficiency. Herein, taking the PBDTTT-C-T:$PC_{71}BM$ PSCs with the PEDOT:PSS and Mo bronzes interfacial layers as an example, the bimolecular recombination status of the cells with different anode interfacial layers was analyzed in virtue of the white light-biased internal quantum efficiency (IQE) measurement. Figure 6, panels a and b display the measured IQE curves of the PBDTTT-C-T:$PC_{71}BM$ PSCs with the PEDOT:PSS and Mo bronzes interfacial layers under different intensities of bias white light. Both of the devices employing the PEDOT:PSS and Mo bronzes annealed at 180 °C as hole extraction layer exhibited more flat IQE response with the highest values of about 70% without bias light. Along with increase of the bias light intensities, the IQE responses of the two devices were gradually decreased, indicating that the bimolecular recombination existed in both devices. Figure 6, panel c illustrates the IQE variance of the two devices as a function of bias light intensity. Relative to the PEDOT:PSS-based device, the Mo bronzes-based device revealed a much slower decrease, indicating that the bimolecular recombination was suppressed to some extent with the Mo bronzes instead of the PEDOT:PSS. This may be attributed to high hole extraction efficiency of the Mo bronzes since the fabrication conditions were identical for the two devices except the anode interfacial layers.

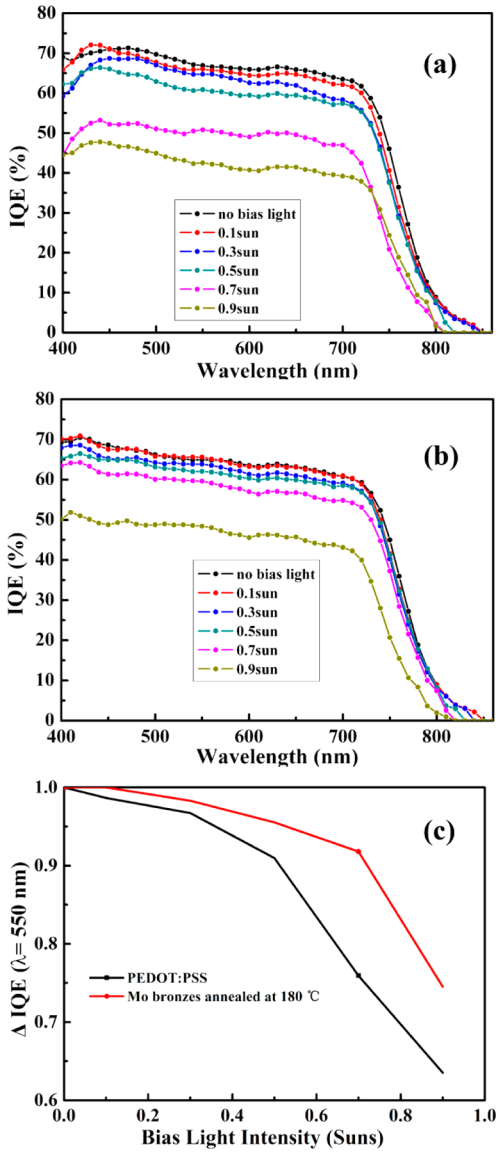

Figure 6. Measured IQEs of the PBDTTT-C-T:$PC_{71}BM$ PSCs using (a) PEDOT:PSS and (b) Mo bronzes annealed at 180 °C as the anode interfacial layers under various intensities of bias white light. (c) The IQE dependence (λ = 550 nm) on bias light intensity for the two kinds of PSCs.

The stability of the PCDTBT:$PC_{71}BM$ BHJ cells with Mo bronzes was also tested in comparison with the control device with PEDOT:PSS interfacial layer. These solar cells were stored in a N_2-filled glovebox without encapsulation, and their photovoltaic performance was measured every certain time at ambient condition. The normalized PCE values of the two devices are plotted as a function of the store time in Figure 7,

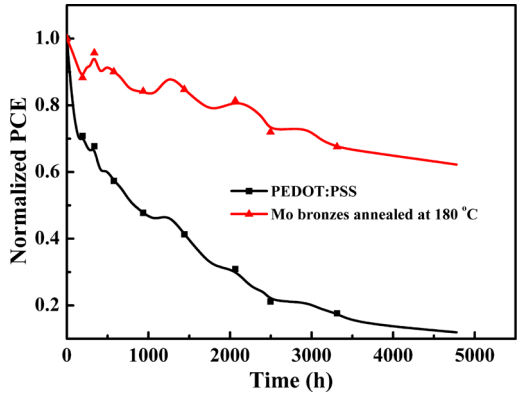

Figure 7. Stabilities of normalized PCE of the PCDTBT:$PC_{71}BM$ PSCs using the PEDOT:PSS and Mo bronzes as the anode interfacial layers, respectively. These nonencapsulated devices were stored in N_2-filled glovebox and measured under ambient condition every certain time.

and the detailed degradations of J_{SC}, FF, and V_{OC} are given in Figure S6 of the Supporting Information. The PCDTBT:$PC_{71}BM$ BHJ cell with Mo bronzes exhibited more enhanced stability than the control device with PEDOT:PSS. The PCE of the Mo bronzes-based cell still maintained more than 62% of its initial value after storing for about 5000 h, with FF and J_{SC} retaining about 92% and 70% of their initial values, respectively. However, the PEDOT:PSS-based cell degraded rapidly, remaining only 11% of the initial PCE after storing for about 5000 h. The FF and J_{SC} values of the PEDOT:PSS-based control device were significantly decreased to 60% and 31.7% of their initial values. These results highlight that the prepared solution-processed Mo bronzes behave as an efficient and stable anode interfacial material. Thanks to its facile and green synthesis and compatibility with roll-to-roll solution-processing, the solution-processed Mo bronzes are expected to be a promising hole extraction material for PSCs.

DOI: 10.1021/acsami.5b02997
ACS Appl. Mater. Interfaces 2015, 7, 13590−13596

4. CONCLUSIONS

In summary, a facile and green one-pot strategy is proposed to synthesize solution-processable Mo bronzes nanoparticles through reducing the fractional self-aggregated ammonium heptamolybdate with mild reducing agent ascorbic acid at low temperatures. The results disclosed that the synthesized Mo bronzes exhibited strong n-type semiconductor characteristics with a work function of 5.2−5.4 eV, and the presented gap states near the Fermi level were beneficial for facilitating hole extraction. The polymer solar cells with the Mo bronzes as anode interfacial layer exhibited remarkably enhanced photovoltaic performance compared to the control cells using the PEDOT:PSS as anode interfacial layer. Moreover, the ambient stability of polymer solar cells was greatly improved by using Mo bronzes to replace PEDOT:PSS as the anode interfacial layer. The facile and green synthesis of solution-processable Mo bronzes nanoparticles and compatibility with low-temperature wet processing render it a promising anode interfacial material for polymer solar cells.

■ ASSOCIATED CONTENT

Supporting Information

Size histogram of as-prepared Mo broznes nanoparticles, absorption spectra of the Mo bronzes solution and the photograph of the Mo bronzes solution, optical band gap (E_g) derived following Tauc's formula, transmittance spectra of Mo bronze, PEDOT:PSS on an ITO/glass substrate, stabilities of the normalized J_{SC}, FF, V_{OC}, and PCE of the PCDTBT:$PC_{71}BM$ PSCs using the PEDOT:PSS and Mo bronzes as the anode interfacial layers. The Supporting Information is available free of charge on the ACS Publications website at DOI: 10.1021/acsami.5b02997.

■ AUTHOR INFORMATION

Corresponding Author

*Phone: +86 431 8526 2819. Fax: +86 431 8526 2126. E-mail: xiezy_n@ciac.ac.cn.

Notes

The authors declare no competing financial interest.

■ ACKNOWLEDGMENTS

This work was supported by the National Basic Research Program of China (973 Project, Grant No. 2014CB643504), the National Natural Science Foundation of China (Nos. 51325303, 51273193, and 21334006), and the Strategic Priority Research Program of the Chinese Academy of Sciences (XDB12030200). J.T.W. also thanks Dr. X. F. Jia and Dr. Q. S. Liang for fruitful discussions.

■ REFERENCES

(1) Service, R. F. Outlook Brightens for Plastic Solar Cells. *Science* **2011**, *332*, 293−293.

(2) Dennler, G.; Scharber, M. C.; Brabec, C. J. Polymer-Fullerene Bulk-Heterojunction Solar Cells. *Adv. Mater.* **2009**, *21*, 1323−1338.

(3) Ameri, T.; Li, N.; Brabec, C. J. Highly Efficient Organic Tandem Solar Cells: A Follow-up Review. *Energy Environ. Sci.* **2013**, *6*, 2390−2413.

(4) Li, N.; Baran, D.; Forberich, K.; Machui, F.; Ameri, T.; Turbiez, M.; Carrasco-Orozco, M.; Drees, M.; Facchetti, A.; Krebs, F. C.; Brabec, C. J. Towards 15% Energy Conversion Efficiency: A Systematic Study of the Solution-Processed Organic Tandem Solar Cells Based on Commercially Available Materials. *Energy Environ. Sci.* **2013**, *6*, 3407−3413.

(5) Machui, F.; Hosel, M.; Li, N.; Spyropoulos, G. D.; Ameri, T.; Sondergaard, R. R.; Jorgensen, M.; Scheel, A.; Gaiser, D.; Kreul, K.; Lenssen, D.; Legros, M.; Lemaitre, N.; Vilkman, M.; Valimaki, M.; Nordman, S.; Brabec, C. J.; Krebs, F. C. Cost Analysis of Roll-to-Roll Fabricated ITO Free Single and Tandem Organic Solar Modules Based on Data from Manufacture. *Energy Environ. Sci.* **2014**, *7*, 2792−2802.

(6) Azimi, H.; Hou, Y.; Brabec, C. J. Towards Low-Cost, Environmentally Friendly Printed Chalcopyrite and Kesterite Solar Cells. *Energy Environ. Sci.* **2014**, *7*, 1829−1849.

(7) Andersen, T. R.; Dam, H. F.; Hosel, M.; Helgesen, M.; Carle, J. E.; Larsen-Olsen, T. T.; Gevorgyan, S. A.; Andreasen, J. W.; Adams, J.; Li, N.; Machui, F.; Spyropoulos, G. D.; Ameri, T.; Lemaitre, N.; Legros, M.; Scheel, A.; Gaiser, D.; Kreul, K.; Berny, S.; Lozman, O. R.; Nordman, S.; Valimaki, M.; Vilkman, M.; Sondergaard, R. R.; Jorgensen, M.; Brabec, C. J.; Krebs, F. C. Scalable, Ambient Atmosphere Roll-to-Roll Manufacture of Encapsulated Large Area, Flexible Organic Tandem Solar Cell Modules. *Energy Environ. Sci.* **2014**, *7*, 2925−2933.

(8) Spyropoulos, G. D.; Kubis, P.; Li, N.; Baran, D.; Lucera, L.; Salvador, M.; Ameri, T.; Voigt, M. M.; Krebs, F. C.; Brabec, C. J. Flexible Organic Tandem Solar Modules with 6% Efficiency: Combining Roll-to-Roll Compatible Processing with High Geometric Fill Factors. *Energy Environ. Sci.* **2014**, *7*, 3284−3290.

(9) Heeger, A. J. 25th Anniversary Article: Bulk Heterojunction Solar Cells: Understanding the Mechanism of Operation. *Adv. Mater.* **2014**, *26*, 10−28.

(10) Ameri, T.; Khoram, P.; Min, J.; Brabec, C. J. Organic Ternary Solar Cells: A Review. *Adv. Mater.* **2013**, *25*, 4245−4266.

(11) Huang, Y.; Kramer, E. J.; Heeger, A. J.; Bazan, G. C. Bulk Heterojunction Solar Cells: Morphology and Performance Relationships. *Chem. Rev.* **2014**, *114*, 7006−7043.

(12) Dou, L.; You, J.; Hong, Z.; Xu, Z.; Li, G.; Street, R. A.; Yang, Y. 25th Anniversary Article: A Decade of Organic/Polymeric Photovoltaic Research. *Adv. Mater.* **2013**, *25*, 6642−6671.

(13) Zhang, Q.; Kan, B.; Liu, F.; Long, G.; Wan, X.; Chen, X.; Zuo, Y.; Ni, W.; Zhang, H.; Li, M.; Hu, Z.; Huang, F.; Cao, Y.; Liang, Z.; Zhang, M.; Russell, T. P.; Chen, Y. Small-Molecule Solar Cells with Efficiency over 9%. *Nat. Photonics* **2015**, *9*, 35−41.

(14) Yusoff, A. R. b. M.; Kim, D.; Kim, H. P.; Shneider, F. K.; da Silva, W. J.; Jang, J. A High Efficiency Solution Processed Polymer Inverted Triple-Junction Solar Cell Exhibiting a Power Conversion Efficiency of 11.83%. *Energy Environ. Sci.* **2015**, *8*, 303−316.

(15) Liu, Y.; Zhao, J.; Li, Z.; Mu, C.; Ma, W.; Hu, H.; Jiang, K.; Lin, H.; Ade, H.; Yan, H. Aggregation and Morphology Control Enables Multiple Cases of High-Efficiency Polymer Solar Cells. *Nat. Commun.* **2014**, *5*, 5293.

(16) Zhao, W.; Ye, L.; Zhang, S.; Fan, B.; Sun, M.; Hou, J. Ultrathin Polyaniline-Based Buffer Layer for Highly Efficient Polymer Solar Cells with Wide Applicability. *Sci. Rep.* **2014**, *4*, 6570.

(17) Xu, B.; Sheibani, E.; Liu, P.; Zhang, J.; Tian, H.; Vlachopoulos, N.; Boschloo, G.; Kloo, L.; Hagfeldt, A.; Sun, L. Carbazole-Based Hole-Transport Materials for Efficient Solid-State Dye-Sensitized Solar Cells and Perovskite Solar Cells. *Adv. Mater.* **2014**, *26*, 6629−6634.

(18) Wong, K. H.; Ananthanarayanan, K.; Luther, J.; Balaya, P. Origin of Hole Selectivity and the Role of Defects in Low-Temperature Solution-Processed Molybdenum Oxide Interfacial Layer for Organic Solar Cells. *J. Phys. Chem. C* **2012**, *116*, 16346−16351.

(19) Wang, F.; Tan, Z. A.; Li, Y. Solution-Processable Metal Oxides/Chelates as Electrode Buffer Layers for Efficient and Stable Polymer Solar Cells. *Energy Environ. Sci.* **2015**, *8*, 1059−1091.

(20) MacLeod, B. A.; Tremolet de Villers, B. J.; Schulz, P.; Ndione, P. F.; Kim, H.; Giordano, A. J.; Zhu, K.; Marder, S. R.; Graham, S.; Berry, J. J.; Kahn, A.; Olson, D. C. Stability of Inverted Organic Solar Cells with ZnO Contact Layers Deposited from Precursor Solutions. *Energy Environ. Sci.* **2015**, *8*, 592−601.

(21) Deng, Y.; Liu, J.; Wang, J.; Liu, L.; Li, W.; Tian, H.; Zhang, X.; Xie, Z.; Geng, Y.; Wang, F. Dithienocarbazole and Isoindigo Based

DOI: 10.1021/acsami.5b02997
ACS Appl. Mater. Interfaces 2015, 7, 13590−13596

Amorphous Low Bandgap Conjugated Polymers for Efficient Polymer Solar Cells. *Adv. Mater.* **2014**, *26*, 471−476.
(22) Subbiah, J.; Purushothaman, B.; Chen, M.; Qin, T.; Gao, M.; Vak, D.; Scholes, F. H.; Chen, X.; Watkins, S. E.; Wilson, G. J.; Holmes, A. B.; Wong, W. W. H.; Jones, D. J. Organic Solar Cells Using a High-Molecular-Weight Benzodithiophene−Benzothiadiazole Copolymer with an Efficiency of 9.4%. *Adv. Mater.* **2014**, 702−705.
(23) Yan, H.; Lee, P.; Armstrong, N. R.; Graham, A.; Evmenenko, G. A.; Dutta, P.; Marks, T. J. High-Performance Hole-Transport Layers for Polymer Light-Emitting Diodes. Implementation of Organosiloxane Cross-Linking Chemistry in Polymeric Electroluminescent Devices. *J. Am. Chem. Soc.* **2005**, *127*, 3172−3183.
(24) Jorgensen, M.; Norrman, K.; Krebs, F. C. Stability/Degradation of Polymer Solar Cells. *Sol. Energy Mater. Sol. Cells* **2008**, *92*, 686−714.
(25) Ratcliff, E. L.; Zacher, B.; Armstrong, N. R. Selective Inter Layers and Contacts in Organic Photovoltaic Cells. *J. Phys. Chem. Lett.* **2011**, *2*, 1337−1350.
(26) Xie, F.; Choy, W. C. H.; Wang, C.; Li, X.; Zhang, S.; Hou, J. Low-Temperature Solution-Processed Hydrogen Molybdenum and Vanadium Bronzes for an Efficient Hole-Transport Layer in Organic Electronics. *Adv. Mater.* **2013**, *25*, 2051−2055.
(27) Meyer, J.; Khalandovsky, R.; Görrn, P.; Kahn, A. MoO_3 Films Spin-Coated from a Nanoparticle Suspension for Efficient Hole-Injection in Organic Electronics. *Adv. Mater.* **2011**, *23*, 70−73.
(28) Cheng, H.; Kamegawa, T.; Mori, K.; Yamashita, H. Surfactant-Free Nonaqueous Synthesis of Plasmonic Molybdenum Oxide Nanosheets with Enhanced Catalytic Activity for Hydrogen Generation from Ammonia Borane under Visible Light. *Angew. Chem., Int. Ed.* **2014**, *53*, 2910−2914.
(29) Dong, W. J.; Jung, G. H.; Lee, J.-L. Solution-Processed-MoO_3 Hole Extraction Layer on Oxygen Plasma-Treated Indium Tin Oxide in Organic Photovoltaics. *Sol. Energy Mater. Sol. Cells* **2013**, *116*, 94−101.
(30) Tan, K.-S.; Chuang, M.-K.; Chen, F.-C.; Hsu, C.-S. Solution-Processed Nanocomposites Containing Molybdenum Oxide and Gold Nanoparticles as Anode Buffer Layers in Plasmonic-Enhanced Organic Photovoltaic Devices. *ACS Appl. Mater. Interfaces* **2013**, *5*, 12419−12424.
(31) Soultati, A.; Douvas, A. M.; Georgiadou, D. G.; Palilis, L. C.; Bein, T.; Feckl, J. M.; Gardelis, S.; Fakis, M.; Kennou, S.; Falaras, P.; Stergiopoulos, T.; Stathopoulos, N. A.; Davazoglou, D.; Argitis, P.; Vasilopoulou, M. Solution-Processed Hydrogen Molybdenum Bronzes as Highly Conductive Anode Interlayers in Efficient Organic Photovoltaics. *Adv. Energy Mater.* **2014**, *4*, 1300896.
(32) Li, X.; Choy, W. C. H.; Xie, F.; Zhang, S.; Hou, J. Room-Temperature Solution-Processed Molybdenum Oxide as a Hole Transport Layer with Ag Nanoparticles for Highly Efficient Inverted Organic Solar Cells. *J. Mater. Chem. A* **2013**, *1*, 6614−6621.
(33) Liu, J.; Shao, S.; Fang, G.; Meng, B.; Xie, Z.; Wang, L. High-Efficiency Inverted Polymer Solar Cells with Transparent and Work-Function Tunable MoO_3-Al Composite Film as Cathode Buffer Layer. *Adv. Mater.* **2012**, *24*, 2774−2779.
(34) Liu, F.; Shao, S.; Guo, X.; Zhao, Y.; Xie, Z. Efficient Polymer Photovoltaic Cells Using Solution-Processed MoO_3 as Anode Buffer Layer. *Sol. Energy Mater. Sol. Cells* **2010**, *94*, 842−845.
(35) Li, X.; Xie, F.; Zhang, S.; Hou, J.; Choy, W. C. H. Over 1.1 eV Workfunction Tuning of Cesium Intercalated Metal Oxides for Functioning as Both Electron and Hole Transport Layers in Organic Optoelectronic Devices. *Adv. Funct. Mater.* **2014**, *24*, 7348−7356.
(36) Li, X.; Xie, F.; Zhang, S.; Hou, J.; Choy, W. C. H. MoO_x and V_2O_x as Hole and Electron Transport Layers through Functionalized Intercalation in Normal and Inverted Organic Optoelectronic Devices. *Light Sci. Appl.* **2015**, *4*, e273.
(37) Girtan, M.; Rusu, M. Role of ITO and PEDOT:PSS in Stability/Degradation of Polymer:Fullerene Bulk Heterojunctions Solar Cells. *Sol. Energy Mater. Sol. Cells* **2010**, *94*, 446−450.
(38) Steirer, K. X.; Ndione, P. F.; Widjonarko, N. E.; Lloyd, M. T.; Meyer, J.; Ratcliff, E. L.; Kahn, A.; Armstrong, N. R.; Curtis, C. J.; Ginley, D. S.; Berry, J. J.; Olson, D. C. Enhanced Efficiency in Plastic Solar Cells via Energy Matched Solution Processed NiO_x Interlayers. *Adv. Energy Mater.* **2011**, *1*, 813−820.
(39) Zhang, J.; Wang, J. T.; Fu, Y. Y.; Zhang, B. H.; Xie, Z. Y. Efficient and Stable Polymer Solar Cells with Annealing-Free Solution-Processible NiO Nanoparticles as Anode Buffer Layers. *J. Mater. Chem. C* **2014**, *2*, 8295−8302.
(40) Bai, S.; Cao, M.; Jin, Y.; Dai, X.; Liang, X.; Ye, Z.; Li, M.; Cheng, J.; Xiao, X.; Wu, Z.; Xia, Z.; Sun, B.; Wang, E.; Mo, Y.; Gao, F.; Zhang, F. Low-Temperature Combustion-Synthesized Nickel Oxide Thin Films as Hole-Transport Interlayers for Solution-Processed Optoelectronic Devices. *Adv. Energy Mater.* **2014**, *4*, 1301460.
(41) Chen, C. P.; Chen, Y. D.; Chuang, S. C. High-Performance and Highly Durable Inverted Organic Photovoltaics Embedding Solution-Processable Vanadium Oxides as an Interfacial Hole-Transporting Layer. *Adv. Mater.* **2011**, *23*, 3859−3863.
(42) Zilberberg, K.; Trost, S.; Schmidt, H.; Riedl, T. Solution Processed Vanadium Pentoxide as Charge Extraction Layer for Organic Solar Cells. *Adv. Energy Mater.* **2011**, *1*, 377−381.
(43) Tao, C.; Ruan, S. P.; Xie, G. H.; Kong, X. Z.; Shen, L.; Meng, F. X.; Liu, C. X.; Zhang, X. D.; Dong, W.; Chen, W. Y. Role of Tungsten Oxide in Inverted Polymer Solar Cells. *Appl. Phys. Lett.* **2009**, *94*, 043311.
(44) Vasilopoulou, M.; Palilis, L. C.; Georgiadou, D. G.; Douvas, A. M.; Argitis, P.; Kennou, S.; Sygellou, L.; Papadimitropoulos, G.; Kostis, I.; Stathopoulos, N. A.; Davazoglou, D. Reduction of Tungsten Oxide: A Path Towards Dual Functionality Utilization for Efficient Anode and Cathode Interfacial Layers in Organic Light-Emitting Diodes. *Adv. Funct. Mater.* **2011**, *21*, 1489−1497.
(45) de Jong, M. P.; van IJzendoorn, L. J.; de Voigt, M. J. A. Stability of the Interface between Indium-Tin-Oxide and Poly(3,4-ethylenedioxythiophene)/Poly(styrenesulfonate) in Polymer Light-Emitting Diodes. *Appl. Phys. Lett.* **2000**, *77*, 2255−2257.
(46) Hancox, I.; Rochford, L. A.; Clare, D.; Walker, M.; Mudd, J. J.; Sullivan, P.; Schumann, S.; McConville, C. F.; Jones, T. S. Optimization of a High Work Function Solution Processed Vanadium Oxide Hole-Extracting Layer for Small Molecule and Polymer Organic Photovoltaic Cells. *J. Phys. Chem. C* **2013**, *117*, 49−57.
(47) Yao, C.; Xu, X.; Wang, J.; Shi, L.; Li, L. Low-Temperature, Solution-Processed Hole Selective Layers for Polymer Solar Cells. *ACS Appl. Mater. Interfaces* **2013**, *5*, 1100−1107.
(48) Griffin, J.; Pearson, A. J.; Scarratt, N. W.; Wang, T.; Lidzey, D. G.; Buckley, A. R. Organic Photovoltaic Devices Incorporating a Molybdenum Oxide Hole-Extraction Layer Deposited by Spray-Coating from an Ammonium Molybdate Tetrahydrate Precursor. *Org. Electron.* **2014**, *15*, 692−700.
(49) Song, J. M.; Ni, X. M.; Gao, L. S.; Zheng, H. G. Synthesis of Metastable H-MoO_3 by Simple Chemical Precipitation. *Mater. Chem. Phys.* **2007**, *102*, 245−248.
(50) Girotto, C.; Voroshazi, E.; Cheyns, D.; Heremans, P.; Rand, B. P. Solution-Processed MoO_3 Thin Films as a Hole-Injection Layer for Organic Solar Cells. *ACS Appl. Mater. Interfaces* **2011**, *3*, 3244−3247.
(51) Fleisch, T. H.; Mains, G. J. An XPS Study of the UV Reduction and Photochromism of MoO_3 and WO_3. *J. Chem. Phys.* **1982**, *76*, 780−786.
(52) Katrib, A.; Benadda, A.; Sobczak, J. W.; Maire, G. XPS and Catalytic Properties of the Bifunctional Supported $MoO_2(H_x)$Ac on TiO_2 for the Hydroisomerization Reactions of Hexanes and 1-Hexene. *Appl. Catal., A* **2003**, *242*, 31−40.
(53) Vasilopoulou, M.; Douvas, A. M.; Georgiadou, D. G.; Palilis, L. C.; Kennou, S.; Sygellou, L.; Soultati, A.; Kostis, I.; Papadimitropoulos, G.; Davazoglou, D.; Argitis, P. The Influence of Hydrogenation and Oxygen Vacancies on Molybdenum Oxides Work Function and Gap States for Application in Organic Optoelectronics. *J. Am. Chem. Soc.* **2012**, *134*, 16178−16187.
(54) Goodenough, J. B. Metallic Oxides. *Prog. Solid State Chem.* **1971**, *5*, 145−399.

DOI: 10.1021/acsami.5b02997
ACS Appl. Mater. Interfaces 2015, 7, 13590−13596